

# Formation of an interconnected network of iron melt at Earth's lower mantle conditions

Crystal Y. Shi<sup>1</sup>, Li Zhang<sup>2,3</sup>, Wenge Yang<sup>2,4</sup>, Yijin Liu<sup>5</sup>, Junyue Wang<sup>2,4</sup>, Yue Meng<sup>6</sup>, Joy C. Andrews<sup>5</sup> and Wendy L. Mao<sup>1,7,8\*</sup>

Core formation represents the most significant differentiation event in Earth's history. Our planet's present layered structure with a metallic core and an overlying mantle implies that there must be a mechanism to separate iron alloy from silicates in the initially accreted material<sup>1,2</sup>. At upper mantle conditions, percolation has been ruled out as an efficient mechanism because of the tendency of molten iron to form isolated pockets at these pressures and temperatures<sup>3-6</sup>. Here we present experimental evidence of a liquid iron alloy forming an interconnected melt network within a silicate perovskite matrix under pressure and temperature conditions of the Earth's lower mantle. Using nanoscale synchrotron X-ray computed tomography, we image a marked transition in the shape of the iron-rich melt in three-dimensional reconstructions of samples prepared at varying pressures and temperatures using a laser-heated diamond-anvil cell. We find that, as the pressure increases from 25 to 64 GPa, the iron distribution changes from isolated pockets to an interconnected network. Our results indicate that percolation could be a viable mechanism of core formation at Earth's lower mantle conditions.

Nearly 50 years ago, a process for core formation involving percolation of liquid iron through a solid, isotropic silicate matrix was proposed<sup>1</sup>. This theory is well developed for the ideal case of a system with a single solid phase consisting of isotropic crystals. The connectivity of the liquid iron alloy is controlled by the ratio of the solid–liquid interfacial energy ( $\gamma_{sl}$ ) and the solid–solid interfacial energy ( $\gamma_{ss}$ ), which is described by the dihedral angle. As the  $\gamma_{sl}/\gamma_{ss}$  ratio decreases, the shape of the melt in a triple junction changes from an isolated sphere to a concave-faced triangular prism. For dihedral angles below  $60^\circ$ , the liquid is fully interconnected and can percolate through the solid irrespective of melt fraction<sup>7</sup>.

A number of previous experimental results have ruled out percolation as a major core formation mechanism for Earth at upper mantle conditions ( $<23$  GPa), on the basis of the observation that the dihedral angle is higher than  $60^\circ$  for silicate/iron-alloy systems, and thus that the iron alloy melt would not be interconnected, as long as the melt fraction is below a critical value. It was found that the dihedral angle decreases to  $71^\circ$  at transition zone conditions<sup>5</sup> (25 GPa), although this value is still above  $60^\circ$ . The decrease was attributed to a change of the solid–liquid interfacial energy due to the phase transition from  $\gamma$ -spinel to silicate perovskite plus magnesiowüstite. At higher pressures, it was reported that dihedral

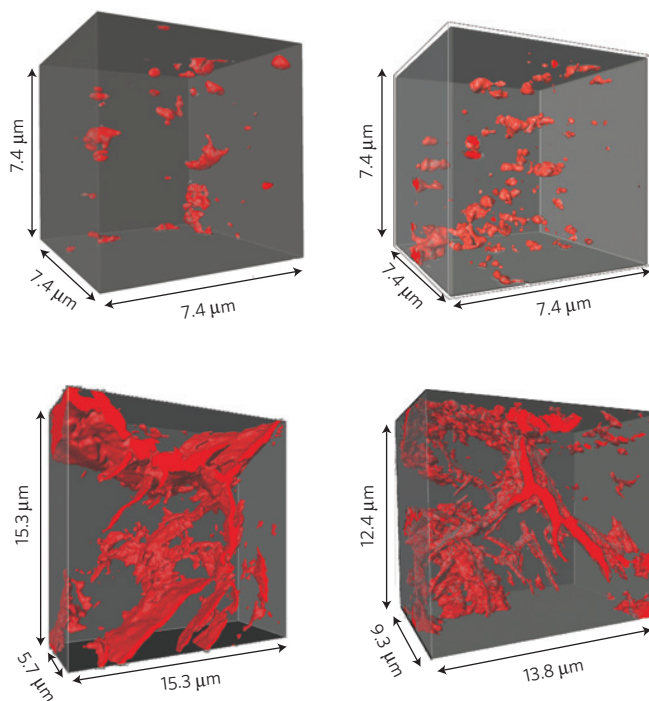


**Figure 1** | 3D distribution of iron alloy melt in silicate perovskite.

**a–d**, Samples were synthesized at 25 GPa (**a**), 39 GPa (**b**), 52 GPa (**c**) and 64 GPa (**d**). The dimensions of each selected volume of interest are labelled.

angles for molten iron decrease to  $51^\circ$  at 47 GPa compared with  $94^\circ$  at 27 GPa (ref. 8), but the results did not demonstrate interconnection of iron melt channels.

In previous measurements, the determination of dihedral angles using transmission electron microscopy or backscattered electron microscopy may not generate satisfactory statistics, especially for high-pressure conditions<sup>9</sup>. Furthermore, when the solid phase is anisotropic, the interfacial energy may vary with crystallographic direction, leading to multiple dihedral angles, which two-dimensional (2D) imaging cannot account

<sup>1</sup>Geological and Environmental Sciences, Stanford University, Stanford, California 94305, USA, <sup>2</sup>Center for High Pressure Science and Technology Advanced Research, Shanghai 201203, China, <sup>3</sup>Geophysical Laboratory, Carnegie Institution of Washington, Washington DC 20015, USA, <sup>4</sup>HPSynC, Geophysical Laboratory, Carnegie Institution of Washington, Argonne, Illinois 60439, USA, <sup>5</sup>Stanford Synchrotron Radiation Lightsource, SLAC National Accelerator Laboratory, Menlo Park, California 94025, USA, <sup>6</sup>HPCAT, Geophysical Laboratory, Carnegie Institution of Washington, Argonne, Illinois 60439, USA, <sup>7</sup>Stanford Institute for Materials and Energy Sciences, SLAC National Accelerator Laboratory, Menlo Park, California 94025, USA, <sup>8</sup>Photon Science, SLAC National Accelerator Laboratory, Menlo Park, California 94025, USA. \*e-mail: [wmao@stanford.edu](mailto:wmao@stanford.edu)

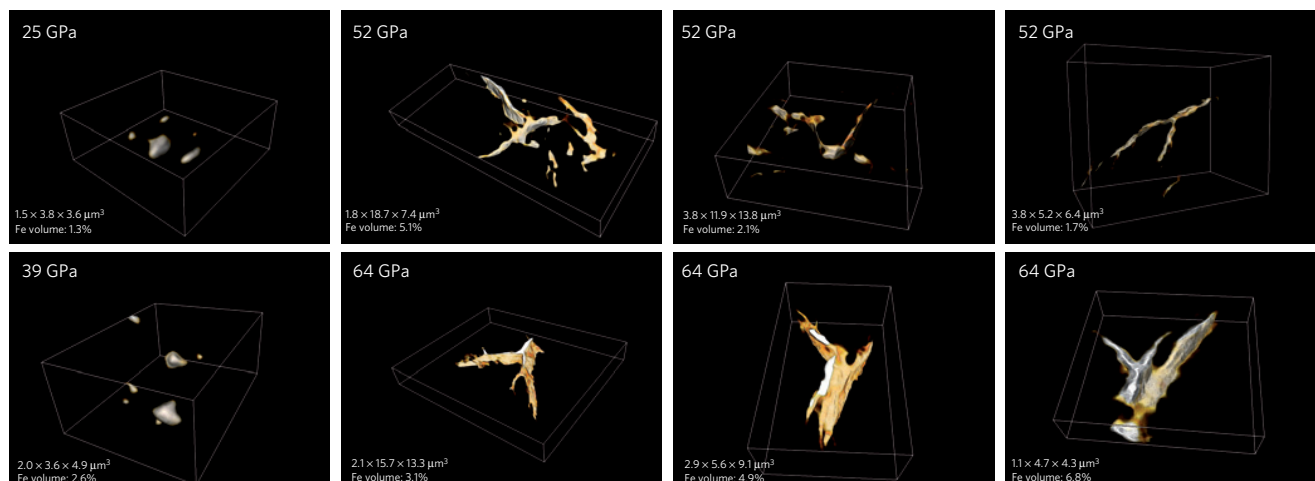


**Figure 2** | Regions of interest in the Fe-melt/silicate sample prepared under different pressure–temperature conditions.

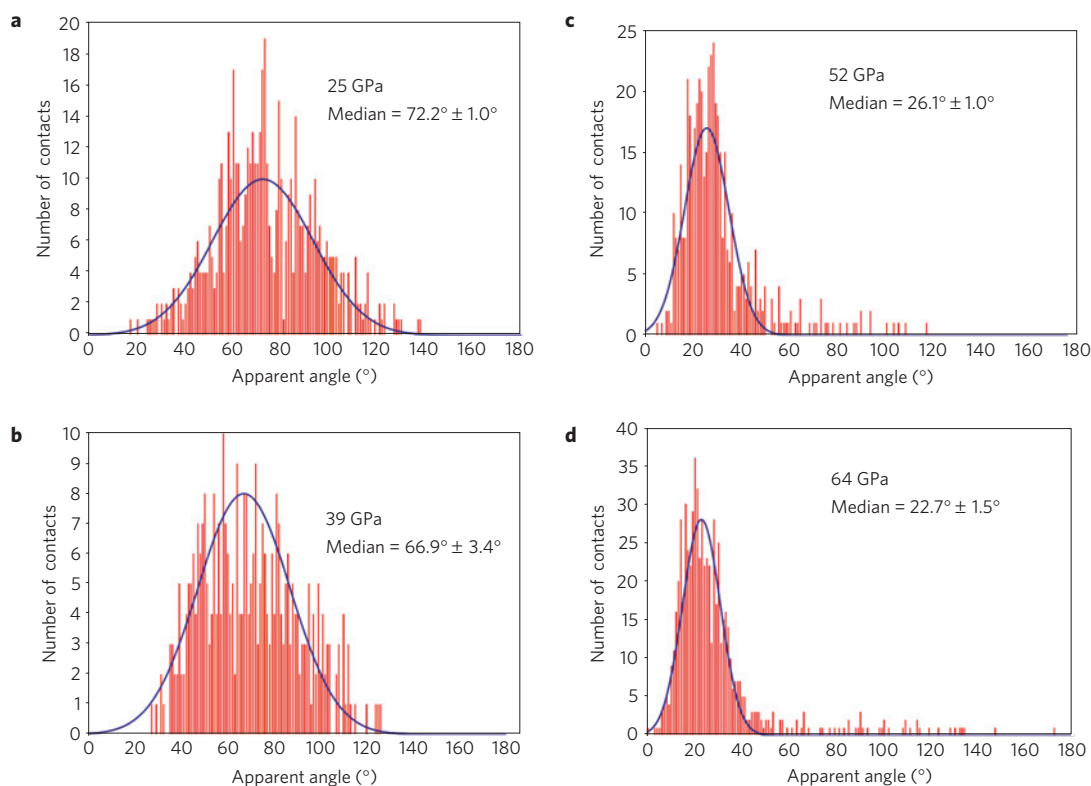


**Figure 3** | Distribution of apparent dihedral angles for contacts between iron alloy melt and silicate perovskite. **a–d**, Samples were synthesized at 25 GPa (**a**), 39 GPa (**b**), 52 GPa (**c**) and 64 GPa (**d**). We report the median value of dihedral angles and the estimated errors based on the 95% confidence interval.

for. To overcome the limitations of traditional 2D-slicing-based approaches, we studied the 3D melt distribution using nanoscale transmission X-ray microscopy (TXM), which is capable of non-destructive 3D imaging at a spatial resolution of a few tens of nanometres, which is necessary for our very small diamond-anvil cell (DAC) samples.

The starting material for our experiments was a mixture of 92 wt% enstatite ( $\text{Mg}_{0.9}\text{Fe}_{0.1}\text{SiO}_3$ ) and 8 wt% iron–nickel–sulphur alloy. Samples were examined *in situ* at high pressures and temperatures in a double-sided laser-heated DAC by synchrotron X-ray powder diffraction. Four samples were first compressed

to different pressures at room temperature. They were then heated to a temperature just below the iron-alloy solidus for 1 h. The samples were then heated to a maximum temperature where the silicates are still solid but the iron alloy was molten<sup>10</sup>, 2,300 K at 25 GPa, 2,800 K at 39 GPa, 3,100 K at 52 GPa and 3,300 K at 64 GPa as confirmed by the loss of the iron-alloy peaks. Supplementary Fig. S1 shows that the diffraction pattern changed from smooth Debye rings to spotty lines, indicating the growth of large perovskite grains. These conditions were then maintained for 3 h to achieve a textural equilibrium, where no further change was revealed from the diffraction patterns, and

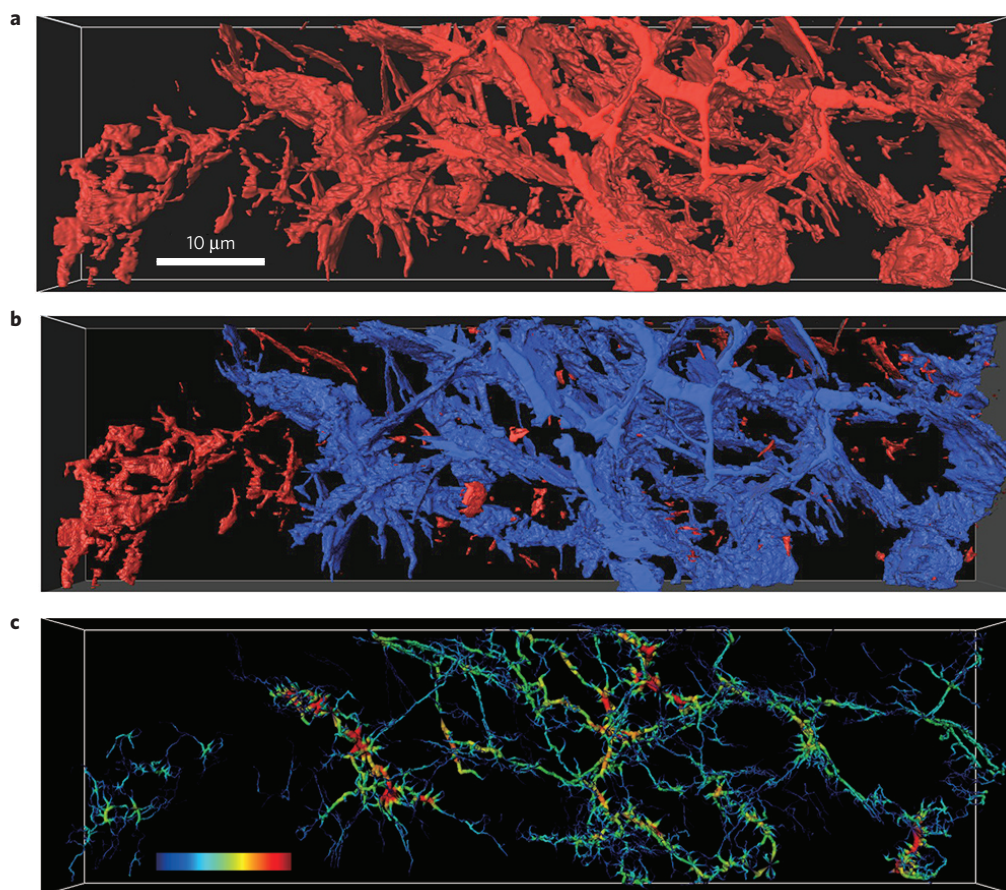


**Figure 4 | 3D renderings of the tomographic reconstruction of the iron alloy melt prepared at 64 GPa.** **a, b**, The channel in **a** at the Fe edge has been confirmed to be iron-rich material by element-sensitive TXM imaging; the channels labelled in blue in **b** are contiguous as determined by using a 3D flood-fill algorithm. **c**, The channel line set extracted from the reconstructed 3D volume; the colour map represents the relative thickness of the channel, with warmer colours indicating thicker channels.

then rapidly quenched to room temperature. The original enstatite recrystallized to form  $(\text{Mg}_{0.9}\text{Fe}_{0.1})\text{SiO}_3$  perovskite in contact with the quenched Fe–Ni–S melt. The rapid temperature quench freezes in the textural relationships between  $(\text{Mg}_{0.9}\text{Fe}_{0.1})\text{SiO}_3$  perovskite and the iron-alloy melt.

X-ray tomography was applied to visualize the recovered samples using a full-field TXM, which is capable of non-destructive imaging with a 30 nm spatial resolution allowing 3D tomographic reconstruction of samples with very small features<sup>11</sup>. As demonstrated in Fig. 1, the iron distribution in the selected regions of interest changes from isolated pockets at 25 and 39 GPa to an interconnected network at 52 and 64 GPa. Figure 2 focuses on local areas of low-melt fraction that changes from the round-shaped melt pockets at 25 and 39 GPa to thin branching shapes at 52 and 64 GPa. The corresponding measurements show a marked dihedral angle reduction in Fig. 3. The small dihedral angle favours percolation. Inter-granular melt feeds and then accumulates into a major network.

An advantage of using this non-destructive 3D imaging technique to investigate the iron-alloy-melt system is that not only does it enable visualization of the entire melt network it also produces more accurate measurements of the dihedral angle. Unlike the 2D-slicing-based approaches, in which the measurement of dihedral angles is strongly dependent on slicing orientation, we are able to visualize the inner structure before performing virtual segmentation on the retrieved 3D data. In this study, the dihedral angles of selected regions of interest are measured on the basis

of least-squares fitting of the vectors normal to the two adjacent surface planes as demonstrated in Supplementary Methods. Ten regions of interest are selected from both samples. The measured dihedral angles range from  $12^\circ \pm 2^\circ$  and  $16^\circ \pm 1^\circ$  for samples at 52 and 64 GPa, respectively, which are much smaller than the critical angle  $60^\circ$ .

Owing to the limited statistics from the 3D approach, we also performed virtual slicing on our 3D data set to measure the 2D apparent angle exhaustively over slices in different depths and different orientations<sup>12</sup>. This provides a direct comparison with published results at lower pressures based on the more traditional method for measuring the apparent angle in a single section and then approximating the true dihedral angle from the distribution of apparent angles. As shown in Fig. 3, the angles measured from the 2D method were estimated to be  $26.1^\circ \pm 1.0^\circ$  and  $22.7^\circ \pm 1.5^\circ$  for samples prepared under 52 and 64 GPa, respectively. The angles measured from samples quenched from 25 and 39 GPa were estimated to be  $72.2^\circ \pm 1.0^\circ$  and  $66.9^\circ \pm 3.4^\circ$ , respectively, which are both above  $60^\circ$ . Whether the dihedral angle decreases or increases slightly with increasing pressure from 52 to 64 GPa, the implication for core formation at these lower mantle pressures is the same—that the melt can be fully interconnected and percolate through the silicates at these conditions.

The 3D rendering and further evaluation of the tomography result over a larger area of the sample prepared at 64 GPa are shown in Fig. 4, providing a better representation of the iron-alloy

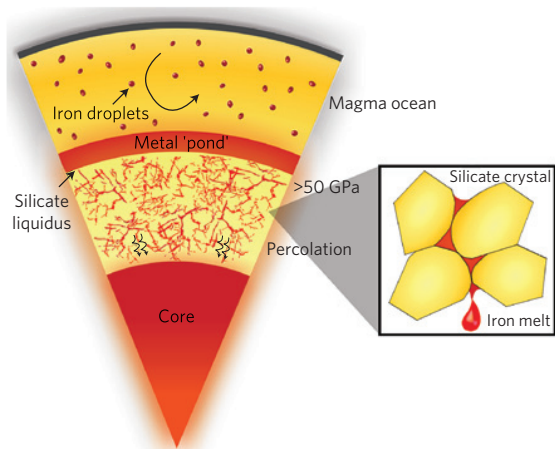


**Figure 5 | Schematic diagram showing possible Earth core formation mechanisms.** Magma ocean and percolation might be dominant mechanisms over different pressure–temperature ranges during Earth’s core formation.

network, which can be seen to spread through both grain edge channels and grain boundary films (Supplementary Movie S1). A 3D flood-fill algorithm-based image segmentation method was used to analyse and visualize the connectivity of the melt network (as shown in Fig. 4b). Starting from user-defined seed points, the surrounding voxels were evaluated to determine whether or not they fulfil the given homogeneity criteria. The voxels were added to the region if they were within the user-defined tolerance. This processing was performed recursively to label the conjoined networks over the given volume. Quantification of the connectivity of the melt network was carried out using a skeletonization algorithm. The cross-sections orthogonal to the channels were systematically reduced to extract the centre lines of the melt channels (as shown in Fig. 4c) from the reconstructed volume. The statistical analysis of the coordination number<sup>13</sup> of all the end nodes was evaluated on the basis of the line set generated by the skeletonization algorithm. Nodes with coordination numbers of 3 and 4 were most abundant.

Less than 3 vol% of the melt formed isolated pockets together with interconnected channels in the samples at 52 and 64 GPa. This may be due to the iron not being uniformly mixed. Previous studies of the silicate perovskite/Fe-alloy system reported the timescale of textural equilibrium as 3 h at 25 GPa and 2,373 K (ref. 6) and approximately 10 min at 24–49 GPa and 2,750–3,050 K (ref. 8). To ensure that our samples reached textural equilibrium, we heated all samples for 4 h (1 h pre-heating +3 h at maximum temperatures), which is longer than the previous studies. Furthermore, the X-ray diffraction patterns of the samples remained unchanged during the later stages of heating. Finally, taking the uncertainties of the dihedral angle calculation into account, the angles are very similar, which is further evidence that the texture of the melt has reached equilibrium.

These results demonstrate that Fe–Ni–S liquid can form an interconnected network in silicate perovskite grain boundaries at pressures above 50 GPa, which indicates a change in the ability of the iron rich melt to percolate through the major lower mantle silicate phase. This change must reflect a decrease in the solid silicate–molten iron interfacial energy with pressure. As the dihedral angle depends on the relative solid–liquid interfacial energy over solid–solid interfacial energy, as the interfacial energy decreases, the liquid is able to spread between the solid grains owing to the minimization of surface energy<sup>14</sup>. The wetting ability of the melt can change as a result of the effect of pressure on interfacial

energy or the effect of pressure on the structures of both the crystalline phase and the liquid iron alloy. Temperature may also have an effect on the interfacial energy<sup>15</sup>, but should not have to be the dominant factor.

Our findings have potential implications for Earth’s early thermal history and the geochemical distribution of elements in the planet. Our planet probably formed from the accretion of a mix of differentiated and undifferentiated bodies<sup>16</sup>. Partial or complete melting of the silicate matrix may be necessary for efficient segregation of core-forming material at this early stage of planetary evolution, because the kilometre-sized planetesimals growing from the solar nebula would not generate high enough pressure conditions for percolation. As Earth accretes and the internal pressure reaches a critical value (above 50 GPa), percolation could become a dominant process. Thus, core formation in our planet may not be a single-stage process, rather it could have occurred as a series of steps under evolving conditions.

Different mechanisms may also operate together during core formation. A possible scenario for Earth’s core formation is illustrated schematically in Fig. 5. At lower pressure conditions, formation of a magma ocean may be the likely differentiation mechanism. Liquid metal can separate rapidly from liquid silicate and accumulates as a ponded layer at the base of the magma ocean. At much higher pressures, percolation will be an efficient mechanism. The ponded iron could then migrate through the underlying silicate mantle towards the proto-core by percolation.

## Methods

The sample mixture was embedded between two layers of MgO that served as a thermal insulator and an internal pressure standard. Laser-heated DAC experiments were performed at 16-IDB of the Advanced Photon Source, Argonne National Laboratory. A laser heating spot (>60 μm in flat top area) was created with a focused yttrium lithium fluoride laser using a double-sided heating technique that minimizes both radial and axial temperature gradients. Temperatures were determined by fitting the thermal radiation from the heating spot to the Planck radiation function<sup>17</sup>. X-ray tomography was conducted at beam line 6-2 of the Stanford Synchrotron Radiation Lightsource.

Received 8 May 2013; accepted 23 August 2013; published online 6 October 2013

## References

1. Elsasser, W. M. in *Earth Science and Meteorites* (eds Geiss, J. & Goldberg, E.) 1–30 (North Holland, 1963).
2. Stevenson, D. J. in *Origin of the Earth* (eds Newsom, H. E. & Jones, J. H.) 231–249 (Oxford Univ. Press, 1990).
3. Shannon, M. C. & Agee, C. B. High pressure constraints on percolative core formation. *Geophys. Res. Lett.* **23**, 2717–2720 (1996).
4. Rubie, D. C., Melosh, H. J., Reid, J. E., Liebske, C. & Righter, K. Mechanisms of metal–silicate equilibration in the terrestrial magma ocean. *Earth Planet. Sci. Lett.* **205**, 239–255 (2003).
5. Shannon, M. C. & Agee, C. B. Percolation of core melts at lower mantle conditions. *Science* **280**, 1059–1061 (1998).
6. Terasaki, H., Frost, D. J., Rubie, D. C. & Langenhorst, F. Percolative core formation in planetesimals. *Earth Planet. Sci. Lett.* **273**, 132–137 (2008).
7. Waff, S. Permeabilities, interfacial areas and curvatures of partially molten systems. *J. Geophys. Res.* **91**, 9261–9276 (1986).
8. Takafuji, N., Hirose, K., Ono, S., Xu, F. & Mitome, M. Segregation of core melts by permeable flow in the lower mantle. *Earth Planet. Sci. Lett.* **224**, 249–257 (2004).
9. Rubie, D. C., Nimmo, F. & Melosh, H. J. Formation of Earth’s core. *Treatise Geophys.* **9**, 51–90 (2007).
10. Shen, G. & Lazor, P. Measurement of melting temperatures of some minerals under lower mantle pressures. *J. Geophys. Res.* **100**, 17699–17713 (1995).
11. Andrews, J. C., Meirer, F., Liu, Y., Mester, Z. & Pianetta, P. Transmission X-ray microscopy for full-field nano imaging of biomaterials. *Microsc. Res. Tech.* **74**, 671–681 (2011).
12. Jurewicz, S. R. & Jurewicz, A. J. G. Distribution of apparent angles on random sections with emphasis on dihedral angle measurements. *J. Geophys. Res.* **91**, 9277–9282 (2012).

13. Zhu, W., Gaetani, G. a, Fusseis, F., Montési, L.G.J. & De Carlo, F. Microtomography of partially molten rocks: Three-dimensional melt distribution in mantle peridotite. *Science* **332**, 88–91 (2011).
14. Smith, C. Some elementary principles of polycrystalline microstructure. *Metallurg. Rev.* **9**, 25–38 (1964).
15. Terasaki, H. *et al.* Interfacial tension of Fe–Si liquid at high pressure: Implications for liquid Fe–alloy droplet size in magma oceans. *Phys. Earth Planet. Int.* **202–203**, 1–6 (2012).
16. Thomas, P.C. *et al.* Differentiation of the asteroid Ceres as revealed by its shape. *Nature* **437**, 224–226 (2005).
17. Meng, Y., Shen, G. & Mao, H.K. Double-sided laser heating system at HPCAT for in situ x-ray diffraction at high pressures and high temperatures. *J. Phys. Condens. Matter* **18**, S1097–S1103 (2006).

### Acknowledgements

W.L.M. and C.Y.S. are supported by NSF-EAR-1055454. Portions of this work were performed at HPCAT (Sector 16), Advanced Photon Source (APS), Argonne National Laboratory. HPCAT operations are supported by DOE-NNSA under Award No. DE-NA0001974 and DOE-BES under Award No. DE-FG02-99ER45775, with partial instrumentation funding by NSF MRI-1126249. APS is supported by DOE-BES, under Contract No. DE-AC02-06CH11357. Portions of this research were carried out at the

SSRL, a Directorate of SLAC National Accelerator Laboratory and an Office of Science User Facility operated for the DOE Office of Science by Stanford University. HPSync is supported by EFree, an Energy Frontier Research Center funded by US Department of Energy (DOE), Office of Science, Office of Basic Energy Sciences (BES) under award number DE-SC0001057.

### Author contributions

W.L.M. proposed this project. C.Y.S. prepared and made measurements on all samples and reconstructed the TXM data. Y.L., J.W., W.Y. and J.C.A. assisted in the TXM data collection. L.Z. synthesized the starting material and assisted with the laser heating experiments. Y.M. assisted with the laser heating experiments. W.L.M. and C.Y.S. analysed the results and wrote the paper. All authors discussed the results and commented on the manuscript.

### Additional information

Supplementary information is available in the [online version of the paper](#). Reprints and permissions information is available online at [www.nature.com/reprints](http://www.nature.com/reprints). Correspondence and requests for materials should be addressed to W.L.M.

### Competing financial interests

The authors declare no competing financial interests.